PAPER • OPEN ACCESS

Parametric study of high-energy ring-shaped electron beams from a laser wakefield accelerator

New Journal of Physics
The open access journal at the forefront of physics

Deutsche Physikalische Gesellschaft DPG
IOP Institute of Physics

Published in partnership with: Deutsche Physikalische Gesellschaft and the Institute of Physics

OPEN ACCESS

RECEIVED
6 July 2021

REVISED
21 November 2021

ACCEPTED FOR PUBLICATION
1 December 2021

PUBLISHED
3 February 2022

PAPER

Parametric study of high-energy ring-shaped electron beams from a laser wakefield accelerator

A Maitrallain[1,*], E Brunetti[1], M J V Streeter[2,3,4], B Kettle[5], R Spesyvtsev[1], G Vieux[1], M Shahzad[1], B Ersfeld[1], S R Yoffe[1], A Kornaszewski[1], O Finlay[3,4], Y Ma[3,4,6], F Albert[7], N Bourgeois[8], S J D Dann[3,8], N Lemos[7], S Cipiccia[9], J M Cole[5], I G González[10], L Willingale[3,4,6], A Higginbotham[11], A E Hussein[6,12], M Šmid[13], K Falk[13,14,15], K Krushelnick[6], N C Lopes[5,16], E Gerstmayr[17], C Lumsdon[11], O Lundh[10], S P D Mangles[5], Z Najmudin[5], P P Rajeev[8], D R Symes[8], A G R Thomas[3,4,6] and D A Jaroszynski[1,*]

[1] SUPA, Department of Physics, University of Strathclyde, Glasgow, United Kingdom
[2] School of Mathematics and Physics, The Queen's University of Belfast, Belfast, BT7 1NN, United Kingdom
[3] Physics Department, Lancaster University, Lancaster LA1 4YB, United Kingdom
[4] The Cockcroft Institute, Keckwick Lane, Daresbury, WA4 4AD, United Kingdom
[5] The John Adams Institute for Accelerator Science, Imperial College London, London, SW72AZ, United Kingdom
[6] Gérard Mourou Center for Ultrafast Optical Science, University of Michigan, Ann Arbor, Michigan 48109, United States of America
[7] Lawrence Livermore National Laboratory, Livermore, CA 94550, United States of America
[8] Central Laser Facility, STFC Rutherford Appleton Laboratory, Didcot OX11 0QX, United Kingdom
[9] Department of Med Phys & Biomedical Eng, University College London, Gower Street, London, United Kingdom
[10] Department of Physics, Lund University, PO Box 118, S-22100, Lund, Sweden
[11] York Plasma Institute, Department of Physics, University of York, York YO10 5DD, United Kingdom
[12] Department of Electrical and Computer Engineering, University of Alberta, Edmonton, Alberta T6G 1H9, Canada
[13] Helmholtz-Zentrum Dresden-Rossendorf, Bautzner Landstraße 400, 01328 Dresden, Germany
[14] Technische Universität Dresden, 01062, Dresden, Germany
[15] Institute of Physics of the ASCR, 18221 Prague, Czech Republic
[16] GoLP/Instituto de Plasmas e Fuso Nuclear, Instituto Superior Tecnico, U.L., Lisboa 1049-001, Portugal
[17] Stanford PULSE Institute, SLAC National Accelerator Laboratory, Menlo Park, CA 94025, United States of America
* Authors to whom any correspondence should be addressed.

E-mail: antoine.maitrallain@strath.ac.uk and d.a.jaroszynski@strath.ac.uk

Keywords: laser–plasma wakefield accelerators, parametric study, annular electron beams

Abstract

Laser wakefield accelerators commonly produce on-axis, low-divergence, high-energy electron beams. However, a high charge, annular shaped beam can be trapped outside the bubble and accelerated to high energies. Here we present a parametric study on the production of low-energy-spread, ultra-relativistic electron ring beams in a two-stage gas cell. Ring-shaped beams with energies higher than 750 MeV are observed simultaneously with on axis, continuously injected electrons. Often multiple ring shaped beams with different energies are produced and parametric studies to control the generation and properties of these structures were conducted. Particle tracking and particle-in-cell simulations are used to determine properties of these beams and investigate how they are formed and trapped outside the bubble by the wake produced by on-axis injected electrons. These unusual femtosecond duration, high-charge, high-energy, ring electron beams may find use in beam driven plasma wakefield accelerators and radiation sources.

1. Introduction

Development of the laser wakefield accelerator (LWFA) has advanced significantly since it was first proposed in 1979 by Tajima and Dawson [1]. Since the first experimental demonstrations of quasi-mono-energetic electron beams in 2004 [2–4], LWFAs have been characterised and shown to have interesting properties, such as tunability, low emittance, high peak current and ultra-short bunch duration. They are particularly

attractive because of their compactness and parameters that compare well with established radio-frequency accelerators. Many of their interesting properties arise from the ultra-small size of their accelerating 'structures'. The laser-excited plasma waves can produce enormous accelerating fields [5] of the order $\approx$100 GV m^{-1}. LWFAs are now becoming valuable tools for scientist. Numerous development programmes aim to find ways of controlling parameters such as reproducibility [6], bunch length [7–9], emittance [10] and energy spread [11]. Making progress will require technological advances in laser technology [6], laser pulse shaping (mode control) [12–14], development of innovative gas targets [7, 15], and fine control of the interaction between laser fields and plasma [16, 17].

A unique aspect of the LWFA is that the shape and velocity of its accelerating structure vary as the laser pulse evolves during its trajectory through the plasma. It can in principle be controlled, which provides a route to controlling the six dimensional (6D) phase-space distribution of the electron beams in and around the accelerating structure. The most common beams produced by LWFAs have narrow divergences of a few mrad; self-injected beams, originating from plasma wave breaking, can accelerate particles to energies exceeding 8 GeV [18], while maintaining relatively small transverse momentum spread and emittance. However, their energy spreads varies between nearly 100% and $<$1%, depending on the injection method [11]. Less well known, but ever present electron beams are 'side electrons', or 'backward emitted' beams [19], which are not injected into the LWFA structure, but nevertheless experience its fields to gain momentum while in the bubble sheath. They appear as low energy (keV to several MeV) very high charge (nC–μC) bunches that are emitted at approximately 45 degrees from the laser axis, or in the counter-propagating direction [19]. These 'side electrons' account for a large fraction of the energy lost by the laser beam to the wake. Several groups have reported observations of unusual ring-shaped (doughnut-shaped) electron beams under different experimental conditions [20–24], and provided various explanations of their origin.

In this paper we present a detailed experimental investigation of the production of high-energy ($\approx$500 MeV) ring shaped beams from a two-stage gas cell [24]. The experimental layout is briefly described, then results of measured electron beams and their spectra are presented. Parametric studies have been conducted to better understand the formation mechanisms behind the generation of these structures and to show that some of their characteristics can be tuned by varying the interaction parameters. In the second section, particle tracking simulations are used to determine the properties of the ring-shaped beams emitted from the LWFA. This is followed by the results of particle-in-cell (PIC) simulations used to develop an understanding of the physical processes underlying the formation of the observed ring structure.

2. Experimental results

2.1. Experimental layout

The experiments have been carried out using the ASTRA-GEMINI laser at the Central Laser Facility, Rutherford Appleton Laboratory. Details of the experimental set-up, shown in figure 1, are presented below [24, 25]. A 4.8–8.4 J, 41–49 fs, high power laser pulse is focused into a dual density gas target using an F/40 off-axis parabola to a spot size of 43 μm full-width-at-half-maximum (FWHM) containing up to 78% of the laser energy, on average, to produce an initial normalised laser vector potential a_0, defined by $8.5 \times 10^{-10}\lambda\,(\mu\text{m})\,\sqrt{I_0[\text{W/cm}^2]}$, between 0.85 and 1.43.

The accelerator medium comprises an additively manufactured, variable length, two-stage gas cell [26]. The first 3 mm long injector cell, filled with He + 2% N_2, is followed by a 1 mm thick slit (to enable the laser pulse to propagate through) and an acceleration stage with variable length (2–21 mm), cell filled with He. The exit wall of the gas cell is tilted at 45 degrees with respect to the vertical enabling modifications of the length of this stage by varying the vertical position of the target. The entrance of the first stage is initially placed at a position that we define as $z = 0$ mm. 25 μm thick, gold coated, Kapton tape is placed immediately after the gas cell to block laser radiation, while allowing the electron beam to be transmitted.

The energy spectra of the electron beams are measured using an electron spectrometer comprising a 0.8 T, 0.1 m long kicker dipole magnet, placed 0.1 m from the source, followed by a 1 T, 0.5 m long, three-component dipole magnet, placed at $z = 0.7$ m. A scintillating Lanex screen is placed at $z = 1.808$ m. This allows characterisation of the electron beam spectral properties, while enabling measurement of the divergence of the beam in the non-dispersion plane. The resolution of the spectrometer at 500 MeV is below 1%. A second Lanex screen is inserted after the weakly dispersive kicker magnet at 0.35 m from the source to directly measure the electron beam profile only when the larger magnet assembly is not on the beam axis.

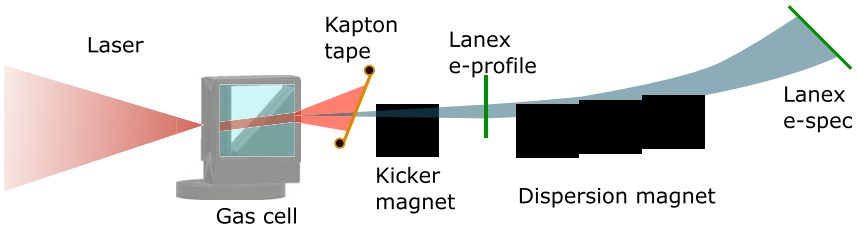

Figure 1. Schematic of the experimental layout. The laser beam is focused into a two-stage, variable length, gas cell. Kapton tape is used to block the laser beam transmitted through the cell. The electron beam is deflected from the axis using an electron spectrometer comprising a weak kicker magnet, a set of three dipole magnets and a Lanex scintillating screen. An additional Lanex screen is inserted before the dipole magnets to directly measure the electron beam profile with minimal spectral dispersion in the horizontal plane, when required.

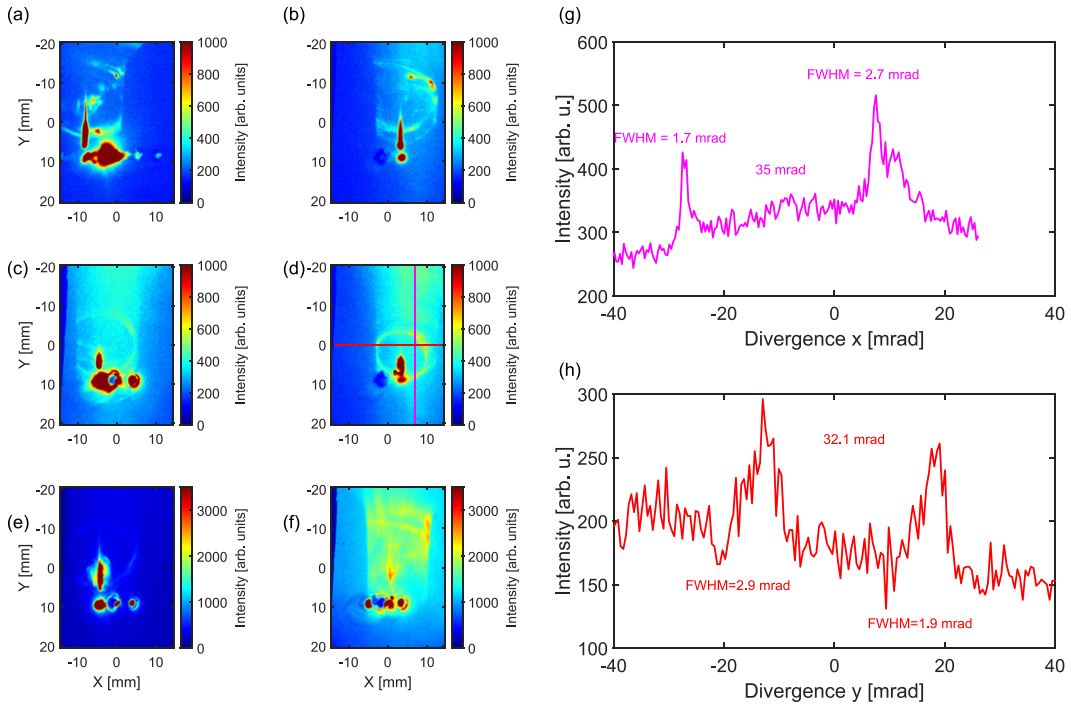

Figure 2. Representative single-shot electron beam profiles measured using the Lanex screen placed after the kicker magnet; (a–f) example images of the ring structured beam for various experimental conditions. Vertical (magenta) and horizontal (red) line-outs of (d) presented in (g) and (h), respectively. The size and FWHM thickness of the ring structure are annotated on plots (g) and (h). The images shown are recorded under the following range of experimental parameters: $0.85 < a_0 < 1.06$, for a laser focused between 1 mm in front of and at the entrance of the gas cell, an acceleration length between 15 and 20 mm and an average electron density $2–4 \times 10^{18}$ cm^{-3}.

2.2. Results

2.2.1. Electron beams

Experimental results show that the on-axis electron beam is often surrounded by a 'ring' structure characterised by a small divergence and energy spread, which appears as a clear annular shape in the spatial distribution and the energy spectrum. In some cases, however, when the energy spread and divergence are large, the structure appears as a halo. Ring and halo features are observed in the beam profile images measured using the Lanex screen after the kicker magnet, as shown in figure 2, for various experimental conditions: a_0 in the range of 0.85 to 1.06, for a laser focused between 1 mm in front of and at the entrance to the gas cell, an acceleration length between 15 and 20 mm, and an average electron density varying from 2 to 4 $\times 10^{18}$ cm^{-3}. Six representative shots are reported in figures 2(a)–(f). Figures 2(g) and (h) show the vertical (magenta) and horizontal (red) line-out, respectively, corresponding to (d). A consistent narrow divergence (compared with the ring radius) central beam is visible in most of the images recorded, but ring structures are only present in some shots for the same experimental conditions. In some cases multiple rings with displaced centres are observed, which may be due to different energies for each ring. The divergence of the rings are 30–60 mrad and their thicknesses are about 2.5 mrad, with small shot-to-shot fluctuations. These results have been obtained at relatively high pressure (700–1000 mbar) gas,

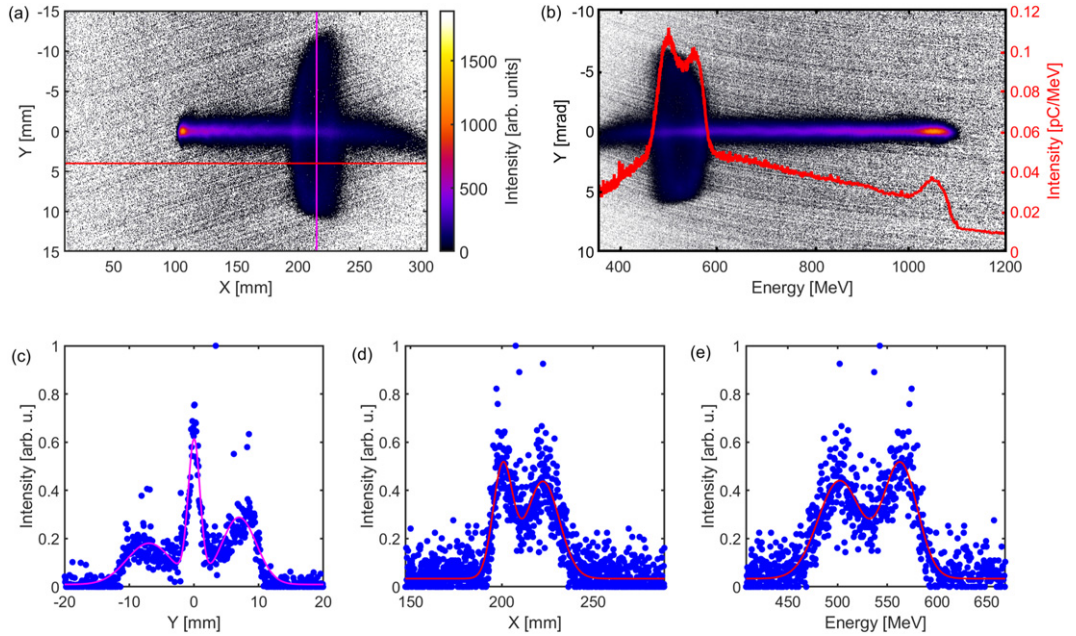

Figure 3. Example of ring like structure measured using the electron spectrometer. (a) Electron spectrum in raw spatial coordinates, with a vertical (magenta) and horizontal (red) line-out shown in (c) and (d), along with a fit to 3 (2) Gaussian distributions in the non-dispersed (dispersed) axes, respectively; (b) electron spectrum plotted in angular/spectral energy coordinates, where the solid red line represents the calibrated spectrum; (e) calibrated horizontal line-out shows the spectrum in MeV. This image is obtained for an initial a_0 of 1.3, a backing pressure of 360 mbar in the first stage and 480 mbar in the second, the laser focused 2 mm inside the gas cell and the acceleration length of 20 mm.

corresponding to an electron density higher than 2×10^{18} cm^{-3}, in the accelerator stage cell and with relatively long accelerating length (>12 mm). The highly saturated parts of the images are due to laser light leaking through holes in the Kapton tape and illuminating the scintillating screens. The line-outs are slightly offset from the centre to clearly distinguish the ring structure.

2.2.2. Electron spectra

The electron beam spectra comprise two parts: (i) a narrow divergence (compared with the ring/halo structure) but broad spectrum, and (ii) the ring beam, as shown in figure 3. This image is obtained for an initial a_0 of 1.3, a backing pressure of 360 mbar in the first stage and 480 mbar in the second (corresponding to an average electron density of 1.2×10^{18} cm^{-3}), with the laser focused 2 mm inside the gas cell and an acceleration length of 20 mm. The figure shows a raw image recorded on the spectrometer Lanex screen (1.808 m from the gas cell) (a) with horizontal (red, dispersion axis) and vertical (magenta) line-outs. This shows that electrons are continuously injected on-axis with relatively small transverse momenta, and also the presence of the 500 MeV ring electron beam. The vertical and horizontal line-outs in (c) and (d) with a fit to 3 (2) Gaussian distributions in the dispersed (non-dispersed) planes, respectively, are included. Panel (b) shows the same data as in (a), but in MeV and mrad, and the spectrum is represented by the solid red line. Figures 3(d) and (e) are line-outs of the respective angular and spectral distributions. The ring appears at 2 different positions on the energy axis in figures 3(b) and (e), which is due to the effect of the divergence of the ring entering the dipole, as will be shown in section 3.1.

The rings, often observed as indistinct halo structures, are only present for accelerator lengths (second stage of the gas cell) exceeding 12 mm and for relatively low pressures (<500 mbar in both stages of the gas target, corresponding to an average electron density less than 1.5×10^{18} cm^{-3}). The line-outs shown in (c) and (d) give ellipse diameters of 12.1 and 7.7 mrad, and an average FWHM thickness of 9.4 and 4 mrad (4 and 1.7 mrad root mean square or RMS) in the dispersed and non-dispersed directions, respectively. Both the radius and the thickness of the ring are larger in the dispersion plane because electrons experience the Lorentz force of the dipole magnet (see discussion below). The relatively narrow width in the dispersion direction indicates that the energy spread for the ring structure is small (<3%) and the thickness in the non-dispersive plane is due to the transverse momentum spread of the ring. A larger energy spread or transverse momentum spread would wash out the ring structure into a halo, as is sometimes observed. The ring radii and thicknesses shown in figure 3 are used to inform the particle tracking simulations presented in the next section. When the gas cell length is reduced, both the energy of the main beam and of the ring decrease, which explains why electron ring structures are only observed for

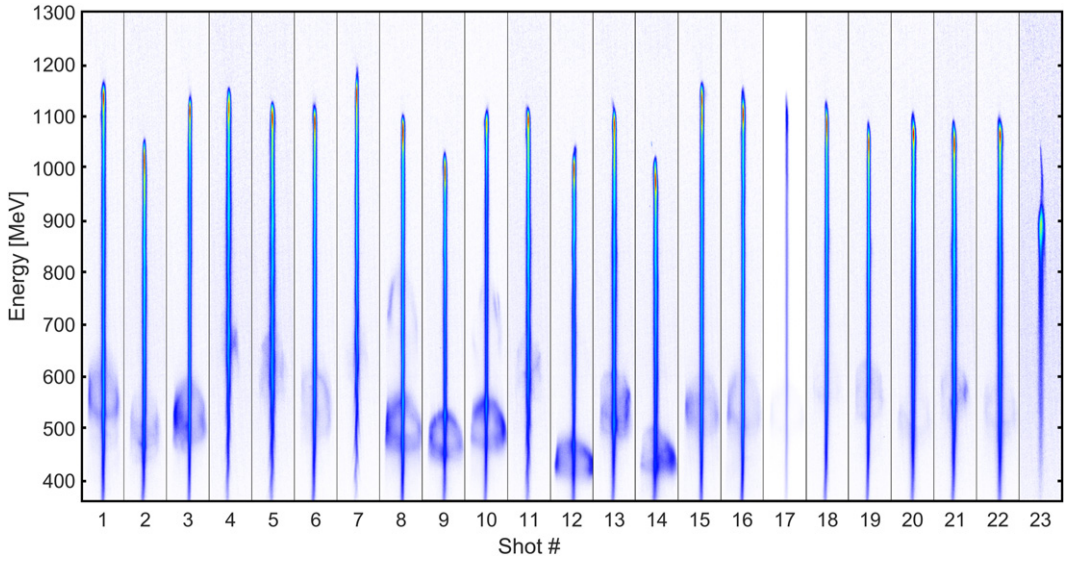

Figure 4. 23 consecutive electron spectrometer images obtained under the same experimental conditions. This shows the stability of the ring/halo electron structure. This data is recorded for an initial a_0 of 1.3, a backing pressure of 360 mbar in the first stage and 480 mbar in the second, the laser focused 2 mm inside the gas cell and an acceleration length of 20 mm.

relatively long gas cells. Below a certain length (≈12 mm), the energy of the halo is below the spectrometer cut-off energy (≈360 MeV) and is therefore not detected.

Ring features are observed in up to 75% of all shots under the most favourable experimental conditions, as reported in figure 4, which shows a series of 23 consecutive images recorded on the spectrometer Lanex screen obtained under the same experimental conditions. A ring or halo structure is not observed on every shot because of fluctuations in parameters such as laser energy (≈1.3%), pulse duration (≈1 fs) and focal spot size (≈3%) and position. The high power laser will also ablate material from the gas cell walls, which causes modifications of the density profile over time. This shows that the ring or halo beam can be accelerated up to 750 MeV under these experimental conditions, for an initial a_0 of 1.3, a backing pressure of 360 mbar in the first stage and 480 mbar in the second, with the laser focused 2 mm inside the gas cell and the acceleration length of 20 mm. Moreover, this figure highlights the generation of several ring/halo structures, which will be discussed in the next section of the paper. Calibration of the scintillator screen indicates that the charge in the ring structures averages at 3.1 ± 2.1 pC RMS and is up to 10 pC, which represents up to 20% of the total charge detected by the spectrometer.

The dependence on the gas cell position relative to the focal spot position is shown in figure 5. The position $z = 0$ mm represents the case where the laser is focused at the entrance to the first stage of the gas cell. This shows that when the focal spot is in front of the entrance to the gas cell ($z < 0$), virtually no electrons are injected on axis and no halo is detected. When the target is moved toward the focal spot ($z < 0$), electrons are injected on-axis. When the focal spot is positioned 2 mm inside the gas cell a halo, and ring structure is observed. Beyond 4 mm into the gas cell, the energy of the halo begins to decrease, indicating that the length over which the halo accelerates, is shortened. This is discussed in more detail in the next section. The same observation is made for the on-axis beam. This set of data is obtained for an initial a_0 of 1.24, a backing pressure of 360 mbar in the first stage and 480 mbar in the second (corresponding to an average electron density over the full length of 1.2×10^{18} cm^{-3}) and acceleration length of 20 mm.

A laser energy scan has also been conducted, presented in figure 6, which shows that the ring-like or halo structures only appear for a given range of a_0 values. At low a_0, no on-axis or halo electrons are produced. When the intensity is increased, on axis electrons are consistently injected and a low energy halo appears; the energy of this halo increases with a_0 initially, but when the laser energy is further increased, to $a_0 > 1.4$, the halo vanishes and only on-axis electrons are observed. This will be discussed in the next section. The energy scan is undertaken for a backing pressure of 360 mbar in the first stage and 480 mbar in the second (corresponding to an average electron density of 1.2×10^{18} cm^{-3}), the laser is focused 2 mm inside the gas cell and the acceleration length is set to 21 mm.

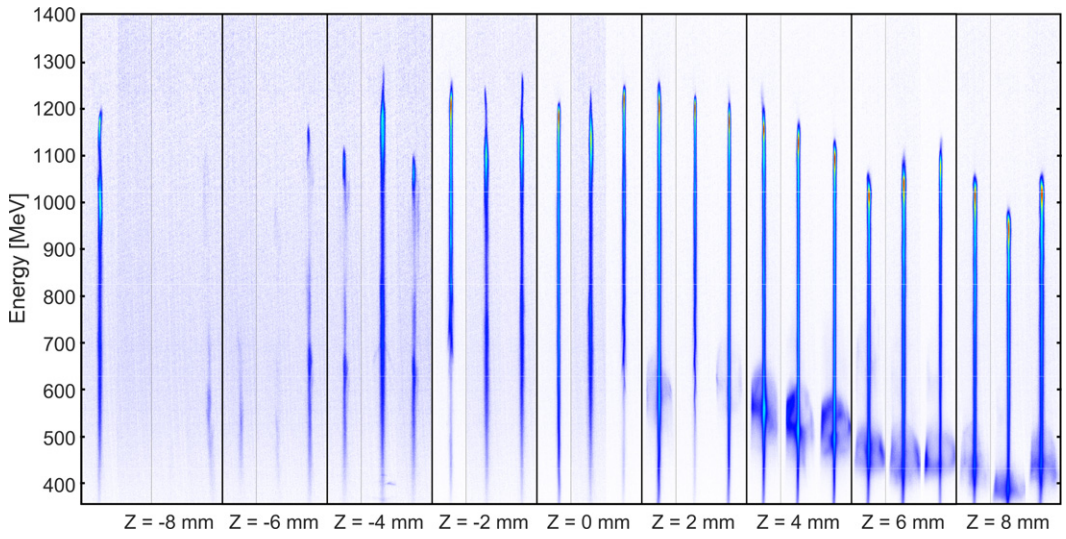

Figure 5. Variation of the position of the focus in the gas cell to investigate its role on electron spectra and appearance of the halo/ring. $z = 0$ mm corresponds to the laser focused at the entrance of the first stage of the gas cell. Negative (positive) values correspond to the laser focused before (after) the gas cell entrance. This set of data is obtained for an initial a_0 of 1.24, a backing pressure of 360 mbar in the first stage and 480 mbar in the second one (corresponding to an average electron density of 1.2×10^{18} cm^{-3}) and an acceleration length of 20 mm.

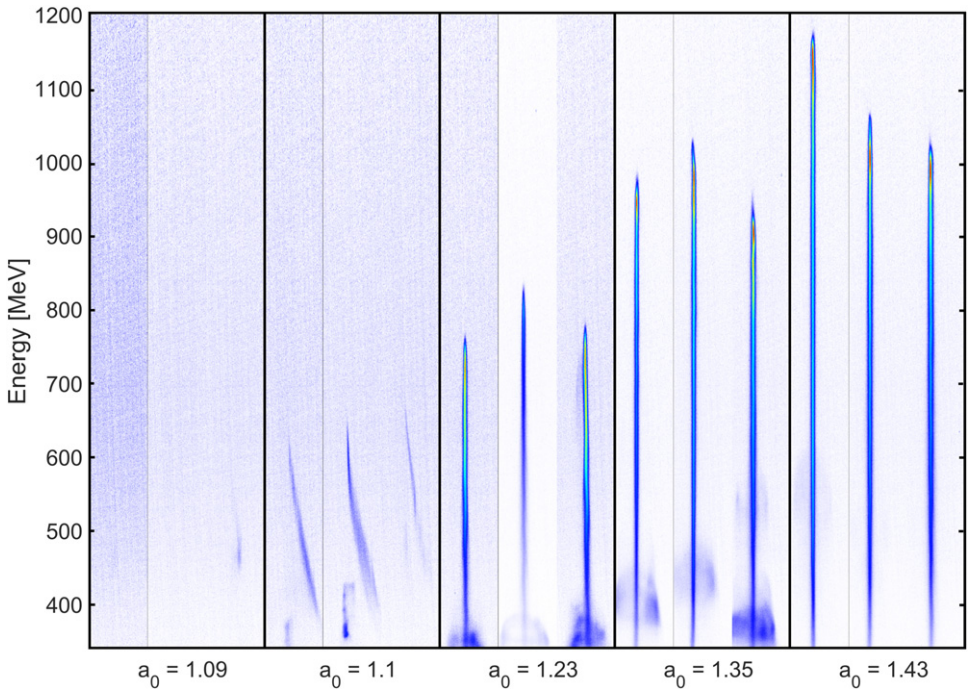

Figure 6. Variation of the initial a_0 to investigate its effect on electron spectra and the appearance of halos/rings. The energy scan is undertaken for a backing pressure of 360 mbar in the first stage and 480 mbar in the second one, (corresponding to an average electron density of 1.2×10^{18} cm^{-3}), the laser focused 2 mm inside the gas cell and an acceleration length set to 21 mm.

3. Numerical simulations

3.1. Particle tracking simulations

Particle tracking simulations have been undertaken to determine the properties of the electron beam emitted from the exit of the LWFA using the general particle tracer (GPT) [27, 28] code, with the objective of reproducing the measurements for the experimental geometry. The layout shown in figure 1 is simulated using GPT with a measured magnetic field map to model the dipole used. The effect of the Kapton tape has been investigated and found to be negligible. The measured shape of the ring structure shown in figure 3 along the non-dispersed axis informed the choice of the divergence (for both the radius and the thickness).

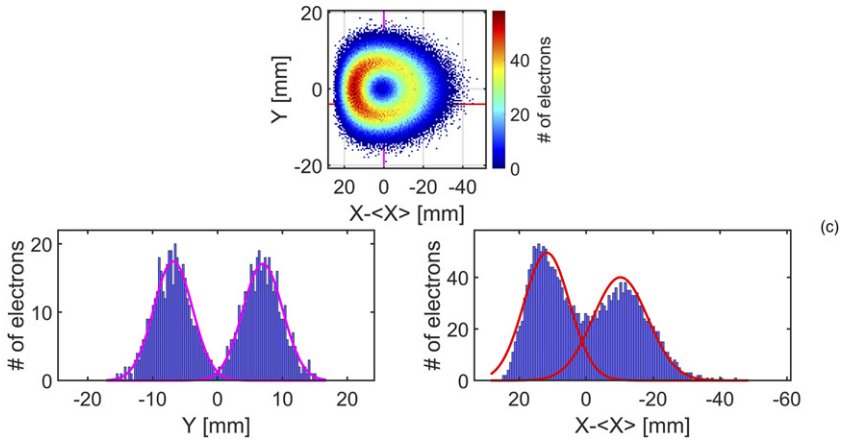

Figure 7. Results of the GPT particle tracking simulations aiming at reproducing the ring shown in figure 3. (a) Histogram plot of the final electron ring structure distribution on the simulated screen and horizontal (red, dispersion axis) and vertical (magenta) line-outs; (b) and (c) vertical and horizontal line-out.

Measurements in the dispersive plane enables the spectral properties (energy and energy spread) to be determined.

A beam energy of 525 MeV and energy spread of 2.5% RMS is used to reproduce the ring beam presented in figure 3. The initial spatial distribution of the electron beam can be estimated from the assumed symmetric Gaussian distribution, which has an RMS width of 5 mm and a ring centred 10 mm from the axis. The divergence corresponding to the measured radius of the ring is 9.2 × 4.2 mrad (dispersive and non-dispersive axis, respectively). The thickness is calculated as 1.75 mrad. The charge simulated in GPT is 5 pC, and self-consistent calculations of space charge forces are enabled but found to be negligible for the energy range, charge and typical divergences. The distributions are shown in figure 7, where (a) is the 2D histogram of the simulated electron distribution evaluated on the screen with the horizontal (red, dispersion axis) and vertical (magenta) line-out presented in (b) and (c), respectively. This figure shows that with these initial parameters the spatial profile of the electron ring structure on the Lanex screen is well described by a bi-Gaussian distribution: the average ring size is 9.8 mrad and its average FWHM thickness is 9.3 × 4 mrad in the dispersed and non-dispersed axis, respectively. This is in very good agreement with the experimentally observed profile reported in figure 3 and suggests that we can use the low energy spreads observed in the ring structure to retrieve the properties of the electron distribution forming the ring structure at the exit of the plasma. The asymmetry observed in both figures 3(d) and 7(c) is due to the dispersion of the dipole varying with the initial divergence of the ring structure.

3.2. PIC simulations

Simulations to reproduce the experimental results have been performed using the quasi-3D PIC code FBPIC [29]. A laser pulse with duration of 40 fs (FWHM) and beam waist $w_0 = 36\ \mu$m, with temporal and transverse Gaussian profile, interacts with a mixture of helium and nitrogen gas. The helium density distribution is uniform over 25 mm (starting at $z = -3$ mm, so the gas cell entrance is assumed to be at $z = 0$ mm) and its density is 6×10^{17} atoms cm^{-3}, comprising both stages of the gas cell. The first stage of the gas cell is 3 mm long with the walls of the cell being 1 mm thick. The nitrogen distribution represents the injection stage and is modeled by a fourth order super-Gaussian centred at $z = 2$ mm, with width of 3 mm (FWHM) and peak density of 2.4×10^{16} atoms cm^{-3}. This results in a density profile with a down ramp, also observed and previously discussed in [22]. Simulations are performed for several laser energies, corresponding to an initial normalised vector potential a_0 between 1.3 and 1.55, and for two positions for the laser focal plane, corresponding to a focus inside the gas cell ($z = 3$ mm), and outside ($z = -3$ mm). The box size is 120 μm in the radial direction and 150 μm in longitudinal direction, with resolutions of 234 nm and 58 nm, respectively. The number of azimuthal modes is 3 and the number of macro-particles (number of atoms which will release electrons after their ionisation) per cell for both gases is 1 in the radial and longitudinal directions and 6 in azimuthal direction.

Simulations performed without nitrogen show that the laser pulse ionises helium and only produces a quasi-linear wakefield. In the presence of nitrogen, however, an electron beam with a broad energy spread is produced in the injection stage and accelerated in the second stage to energies of up to 1.4 GeV through ionization injection. This electron beam drives a strongly nonlinear wakefield, resulting in the formation of several accelerating buckets in addition to the wakefield excited by the laser, as shown in figure 8. The

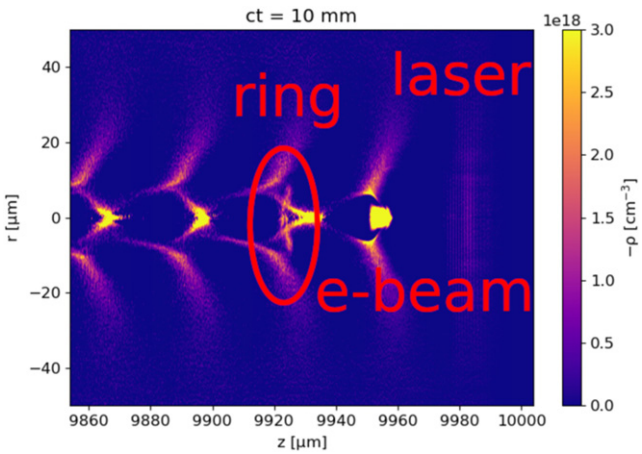

Figure 8. Electron density distribution obtained using FBPIC shows both the ring-shaped and the on-axis electron beams produced by a laser pulse with an initial $a_0 = 1.35$ focused inside the gas cell (at $z = 3$ mm). This snapshot is taken after 10 mm propagation.

accelerating field in these additional buckets is of the order of 20 GV m^{-1}, but this value depends on the laser intensity and electron density. Electrons ionised from nitrogen stream backwards and are deflected off-axis by the dense sheath of electrons surrounding the buckets, becoming trapped in the exterior accelerating field of the laser-generated wakefield, which results in a ring-shaped electron beam. Although this mechanism was originally discussed in [21, 22], here we undertake a systematic parametric study of the ring beams in a higher energy range.

The ring appears when the accelerating structure trailing the electron beam is fully formed. For $a_0 = 1.35$, this occurs at $z = 5$ mm, when the laser is focused inside the cell ($z = 3$ mm) and at $z = 6$ mm, when the laser is focused outside ($z = -3$ mm). In both cases the initial energy spectrum of the ring-shaped beam is broad, extending up to 250 MeV. The length of the first accelerating bucket slowly oscillates during propagation as the electron beam is accelerated by the wake, resulting in a slow expansion and contraction of the transverse size of the ring. When the laser is focused outside the cell, the first bucket gradually shrinks and electrons slip inside the second bucket at $z = 11$ mm, resulting in a filled beam with no ring structure. In this case the charge of the driving electron beam is about 90 pC. When the laser focus is inside the cell, on the other hand, the charge of the driving electron beam is about 140 pC and the size of the first bucket is larger, allowing the ring structure to be preserved and accelerated until the end of the gas cell. Part of the beam will be bunched in the accelerating bucket and produce a narrow energy spike. The charge of the on-axis beam determines the size of the bucket where ring electrons are accelerated, and the acceleration length. These simulation results reproduce what is observed experimentally and reported in figure 5 where no ring or halo structures are observed when the laser is focused in front of, or at the entrance of the gas cell. The discrepancies obtained in the charge estimation are due to the incomplete knowledge of the experimental parameters when modeling the experiment with PIC simulations i.e. the precise density profile. The same mechanism can result in the production of additional ring-shaped beams of lower energy around the accelerating buckets further behind the laser, as observed experimentally and shown in figure 4.

The final electron distribution of the ring-shaped beam is shown in figure 9 for both laser focus positions along with a 3 dimensional representation for the latter case. A ring with a radius of 13 μm and thickness of 11 μm is observed when the laser beam is focused inside the gas cell, whereas no halo is observed when focused outside. The energy spectrum, including both the driving electron beam and the ring-shaped beam, is shown in figure 10 for several laser energies and focus positions to reproduce the trends observed in the scans presented in figures 5 and 6. Note that the measured ring structures are due to the ring shaped momentum distribution. For $a_0 = 1.3$ and $a_0 = 1.35$ a peak with energy between 400 MeV and 500 MeV, energy spread of about 7% and charge of about 40 pC, which corresponds to 30% of the total charge, is formed when the laser is focused inside the gas cell. As can be seen from figures 9(a) and 10(a), no ring structures are formed when the laser is focused before the entrance of the gas cell. The spectrum observed at ≈500 MeV in figure 10(a) with $a_0 = 1.55$ are electrons from the first bunch and no clear ring structure is observed. It starts to develop at $z \approx 8$ mm, as electrons bunch during acceleration in the quasi-linear wakefield excited by the laser. These simulations results are in good quantitative agreement with the experimental and particle tracking simulation results reported in figures 3 and 7. The small discrepancy

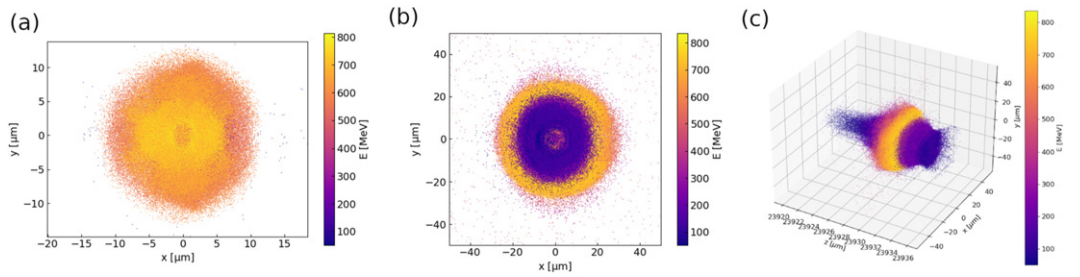

Figure 9. Results of FBPIC simulations showing the spatial distribution of electrons accelerated behind the on-axis electron beam by a laser pulse with $a_0 = 1.35$ focused (a) outside ($z = -3$ mm) and (b) inside the gas cell ($z = 3$ mm). The snapshots are taken after 24 mm propagation. (c) Corresponds to a three-dimensional representation of (b).

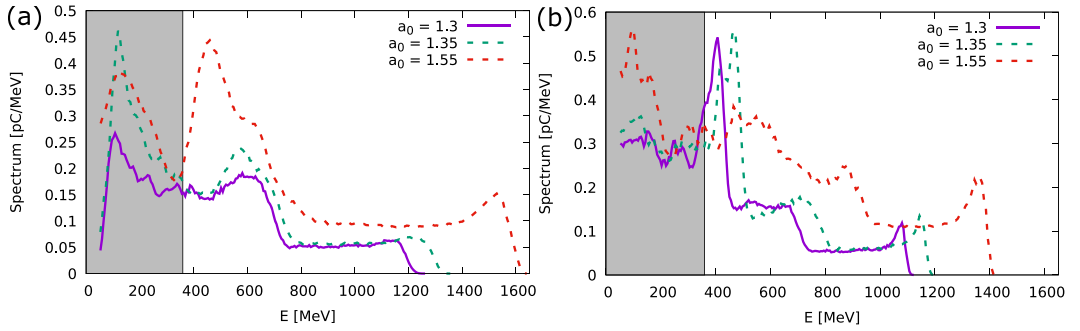

Figure 10. Results of FBPIC simulations showing the final energy spectra of electrons accelerated in the first two buckets by a laser pulse with varying a_0 focused outside (a) ($z = -3$ mm) and inside (b) the gas cell ($z = 3$ mm). The shaded area left of the vertical line represents the region of the spectrum that cannot be accessed by our measurement due to the spectrometer cut off.

observed in the energy spread estimation compared to the results shown in the previous section is due to the assumptions made when modeling the experiment with PIC simulations i.e. on the precise density profile. It is worth noting that similar results are obtained when using a density down ramp where a helium density of 7.5×10^{17} atoms cm^{-3} is used in the first stage and 6×10^{17} atoms cm^{-3} in the second. Another simulation run with a constant effective electron density (where the helium density is decreased in the first stage) shows that the density down ramp between the two stages helps preserve the ring structure in the transition from the first to the second stage, preventing it from diverging, as previously discussed in [22].

For $a_0 = 1.55$, a ring structure is still formed, but the energy spread is broader and the divergence larger. In this case, the laser is sufficiently intense to produce an ion cavity, resulting in a strongly nonlinear wakefield and additional on-axis injection. This is, once more, very similar to that experimentally observed as reported in figure 6 where no ring or halo structures are observed outside the range of a_0 values between 1.23 and 1.35 limit in the energy range accessible. Here, the increase in divergence of the halo/ring structure is not observed as predicted by the PIC simulation because as the images on this diagnostic are relatively noisy, even after background subtraction, increasing the divergence of this pattern will lead to its extinction.

A simulation has also been performed for parameters matching the experimental results presented in section 2.2.1. The helium density is 1.2×10^{18} atoms cm^{-3} in both stages of the gas cell and the laser is focused at the entrance of the gas cell ($z = 0$ mm) with $a_0 = 0.9$. A ring structure containing a charge of about 1.3 pC is formed and accelerated to an energy of about 230 MeV after 9 mm propagation. The beam, however, is subsequently decelerated to about 100 MeV and starts diverging at $z \approx 14$ mm due to the expansion of the accelerating structure. For this higher plasma density an ion cavity is formed and injection takes place also in the second stage of the gas cell. This is also in good agreement with the experimental findings presented in figure 2.

In general, we find that the formation and general properties of the ring depend weakly on the shape of the density profile and the effect of the simulation grid resolution is even weaker. When varying the grid size, variations of the order of 10% in energy and charge are observed but the main features and trends presented are similar. The boundary conditions do not affect the simulations results. On the other hand, finer details, such as position and width of the energy peaks, show a stronger variation. More precise modeling of the experiment would require accurate gas density measurements, which were not available at the time of this experiment. These simulations show that the charge of the ring structured electron beam is

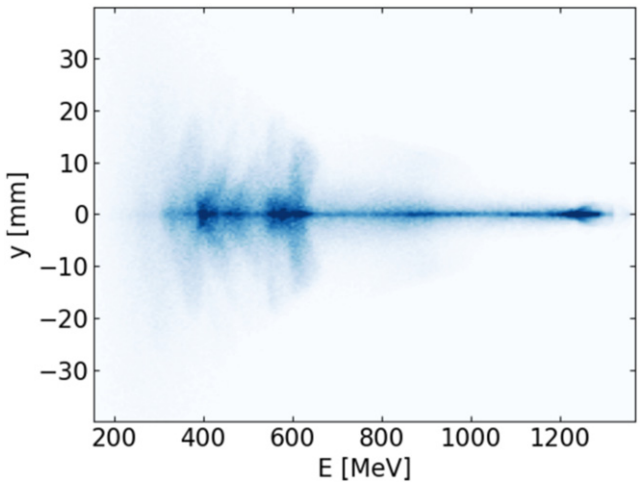

Figure 11. Electron spectrum obtained from FBPIC simulations reported in figures 9(b) and 10(b) transported using GPT through a set up reproducing the experimental one.

proportional to the gas density. Therefore, it may be possible to precisely reproduce the charge of the experiment by reducing the density. However, the beam energy typically increases when the density is decreased. To control both the charge and the energy, the density profile should also be changed, or the density of the first and second stages should be adjusted independently. This requires better knowledge of the gas density profile used in the experiments.

The electron beam with a distribution presented in figures 9(b) and 10(b) is transported using GPT through a beam line that reproduces the experimental set up. The simulated electron spectrum is shown in figure 11 where the halo around the main beam is clearly visible. However, the formation of a clear ring is prevented by the relatively large energy spread obtained in the PIC simulation (7%, compared to the 2.5% obtained from the particle tracking simulations presented in section 3.1).

4. Conclusions

In conclusion, the observation of ring like structures associated with on axis electron injection has been demonstrated experimentally and compared with PIC simulations. Parametric studies have been conducted that demonstrate a level of control on the appearance of these structure and ability to tune some of their properties. Particle tracking simulations have been performed, which enables the distribution of the particles forming these structures to be determined (after exiting the plasma). PIC simulations enable an understanding of the injection mechanism and beam evolution leading to the formation of the observed features. Ring-like beams may be of interest for transporting currents higher than the Alfvén limit [30] because of their hollowed shapes specifically in the case of lower energy electrons. The fields they transport can be used to collimate relativistic proton bunches [31, 32] and other charged particles as positrons or the production of unique mode structured x-ray beams.

Acknowledgments

The authors would like to thank UK EPSRC (EP/J018171/1, EP/J500094/1, EP/N028694/1), the European Union's Horizon 2020 research and innovation program under Grant Agreement No. 871124 Laserlab-Europe, EuPRAXIA (653782) and the Science and Technology Facilities Council (Cockcroft Institute, ST/G008248/1, ST/P002056) for their support. The author acknowledge the funding from the ST/P000835/1 (John Adams Institute), and the United States Department of Energy Grant No. DE-NA0002372. This work was partially supported by EuCARD-2 (Grant No. 312453), the extreme light infrastructure (ELI) European Project, and by FCT - Fundacao para a Ciencia e a Tecnologia, 15/17 Ministerio da Ciencia e Ensino Superior, Portugal under the Contract POCI/FIS/59574/2004 and by the auspices of the US Department of Energy by Lawrence Livermore National Laboratory under the Contract DE-AC52- 07NA27344, as well as Lawrence Livermore National Security, LLC, and DOE Early Career Research Prog. SCW1575/1. LLNL-JRNL-742178.

Author contribution

The experiment was conceived by AEH, AGRT, FA and SPDM and was conducted by AEH, MJVS, BK and YM, with assistance from SJDD, NB, SC, JMC, EG, IGG, NL, NCL, CL, MS, RS, DRS, GV and DAJ. The data were analyzed by AM, EB, DAJ and RS, with assistance from MJVS, BE, SRY, AK and OF. AH, KF, DAJ, KK, OL, ZN, PPR and LW contributed to planning and interpretation. The manuscript was written by AM, EB and DAJ. All authors reviewed the manuscript.

Data availability

Data associated with research published in this paper is available at https://doi.org/10.15129/75e09e94-376e-481f-85dc-c02d4a63c1e7.

ORCID iDs

M J V Streeter https://orcid.org/0000-0001-9086-9831
B Kettle https://orcid.org/0000-0003-4424-4448
B Ersfeld https://orcid.org/0000-0001-5597-9429
S R Yoffe https://orcid.org/0000-0002-6723-4990
O Finlay https://orcid.org/0000-0002-0026-6584
Y Ma https://orcid.org/0000-0002-3919-4856
N Lemos https://orcid.org/0000-0002-6781-5672
M Šmid https://orcid.org/0000-0002-7162-7500
K Falk https://orcid.org/0000-0001-5975-776X
K Krushelnick https://orcid.org/0000-0001-9116-9511
E Gerstmayr https://orcid.org/0000-0003-1164-8593
S P D Mangles https://orcid.org/0000-0003-2443-4201
Z Najmudin https://orcid.org/0000-0001-6323-4005
A G R Thomas https://orcid.org/0000-0003-3206-8512

References

[1] Tajima T and Dawson J M 1979 Laser electron accelerator *Phys. Rev. Lett.* **43** 267–70
[2] Mangles S P D *et al* 2004 Monoenergetic beams of relativistic electrons from intense laser–plasma interactions *Nature* **431** 535–8
[3] Geddes C G R, Toth C, van Tilborg J, Esarey E, Schroeder C B, Bruhwiler D, Nieter C, Cary J and Leemans W P 2004 High-quality electron beams from a laser wakefield accelerator using plasma-channel guiding *Nature* **431** 538–41
[4] Faure J, Glinec Y, Pukhov A, Kiselev S, Gordienko S, Lefebvre E, Rousseau J-P, Burgy F and Malka V 2004 A laser-plasma accelerator producing monoenergetic electron beams *Nature* **431** 541–4
[5] Pukhov A and Meyer-ter-Vehn J 2002 Laser wake field acceleration: the highly non-linear broken-wave regime *Appl. Phys. B: Lasers Opt.* **74** 355–61
[6] Maier A R *et al* 2020 Decoding sources of energy variability in a laser plasma accelerator *Phys. Rev.* X **10** 031039
[7] Tooley M P, Ersfeld B, Yoffe S R, Noble A, Brunetti E, Sheng Z M, Islam M R and Jaroszynski D A 2017 Towards attosecond high-energy electron bunches: controlling self injection in laser wakefield accelerators through plasma density modulation *Phys. Rev. Lett.* **119** 044801
[8] Islam M R *et al* 2015 Near-threshold electron injection in the laser–plasma wakefield accelerator leading to femtosecond bunches *New J. Phys.* **17** 093033
[9] Lundh O *et al* 2011 Few femtosecond, few kiloampere electron bunch produced by a laser–plasma accelerator *Nat. Phys.* **7** 219–22
[10] Brunetti E *et al* 2010 Low emittance, high brilliance relativistic electron beams from a laser–plasma accelerator *Phys. Rev. Lett.* **105** 215007
[11] Wiggins S M *et al* 2010 High quality electron beams from a laser wakefield accelerator *Plasma Phys. Control. Fusion* **52** 124032
[12] Vieira J and Mendonça J T 2014 Nonlinear laser driven donut wakefields for positron and electron acceleration *Phys. Rev. Lett.* **112** 215001
[13] Mendonça J T and Vieira J 2014 Donut wakefields generated by intense laser pulses with orbital angular momentum *Phys. Plasmas* **21** 033107
[14] He Z-H, Hou B, Lebailly V, Nees J A, Krushelnick K and Thomas A G R 2015 Coherent control of plasma dynamics *Nat. Commun.* **6** ncomms8156
[15] Pak A, Marsh K A, Martins S F, Lu W, Mori W B and Joshi C 2010 Injection and trapping of tunnel ionized electrons into laser produced wakes *Phys. Rev. Lett.* **104** 025003
[16] Mirzaie M *et al* 2015 Demonstration of self-truncated ionization injection for GeV electron beams *Sci. Rep.* **5** 14659
[17] Irman A, Couperus J P, Debus A, Köhler A, Krämer J M, Pausch R, Zarini O and Schramm U 2018 Improved performance of laser wakefield acceleration by tailored self-truncated ionization injection *Plasma Phys. Control. Fusion* **60** 044015
[18] Gonsalves A J *et al* 2019 Petawatt laser guiding and electron beam acceleration to 8 GeV in a laser-heated capillary discharge waveguide *Phys. Rev. Lett.* **122** 084801

[19] Yang X et al 2017 Three electron beams from a laser–plasma wakefield accelerator and the energy apportioning question Sci. Rep. 7 43910
[20] Pollock B B et al 2011 Demonstration of a narrow energy spread, 0.5 GeV electron beam from a two stage laser wakefield accelerator Phys. Rev. Lett. 107 045001
[21] Pollock B B et al 2015 formation of ultrarelativistic electron rings from a laser wakefield accelerator Phys. Rev. Lett. 115 055004
[22] Zhao T Z et al 2016 High flux femtosecond x ray emission from controlled generation of annular electron beams in a laser wakefield accelerator Phys. Rev. Lett. 117 094801
[23] Behm K et al 2019 Measurements of electron beam ring structures from laser wakefield accelerators Plasma Phys. Control. Fusion 61 065012
[24] Spesyvtsev R et al 2019 Generation of electron high energy beams with a ring like structure by a dual stage laser wakefield accelerator Relativistic Plasma Waves and Particle Beams as Coherent and Incoherent Radiation Sources III vol 11036 (International Society for Optics and Photonics) p 110360F
[25] Hussein A E et al 2019 Laser-wakefield accelerators for high-resolution x-ray imaging of complex microstructures Sci. Rep. 9 3249
[26] Vargas M et al 2014 Improvements to laser wakefield accelerated electron beam stability, divergence, and energy spread using three-dimensional printed two-stage gas cell targets Appl. Phys. Lett. 104 174103
[27] Geer S B V D and Loos M J D 2002 General particle tracer (http://pulsar.nl/gpt)
[28] van der Geer S B, Luiten O J, de Loos M J, Pöplau G and van Rienen U 2003 3D space-charge model for GPT simulations of high-brightness electron bunches TESLA Report DESY
[29] Lehe R, Kirchen M, Andriyash I A, Godfrey B B and Vay J-L 2016 A spectral, quasi-cylindrical and dispersion-free Particle-In-Cell algorithm Comput. Phys. Commun. 203 66–82
[30] Davies J R 2003 Magnetic-field-limited currents Phys. Rev. E 68 037501
[31] Stancari G, Valishev A, Annala G, Kuznetsov G, Shiltsev V, Still D A and Vorobiev L G 2011 Collimation with hollow electron beams Phys. Rev. Lett. 107 084802
[32] Fitterer M, Stancari G, Alexander V, Redaelli S and Valuch D 2021 Resonant and random excitations on the proton beam in the large Hadron collider for active halo control with pulsed hollow electron lenses Phys. Rev. Accel. Beams 24 021001